Using Host Galaxy Spectroscopy to Explore Systematics in the Standardisation of Type Ia Supernovae

M. Dixon[1], C. Lidman[2,3], J. Mould[1], L. Kelsey[4,5], D. Brout[6], A. Möller[1], P. Wiseman[5], M. Sullivan[5], L. Galbany[7,8], T. M. Davis[9], M. Vincenzi[4,5], D. Scolnic[10], G. F. Lewis[11], M. Smith[5], R. Kessler[12,13], A. Duffy[1], E. N. Taylor[1], C. Flynn[1], T. M. C. Abbott[14], M. Aguena[15], S. Allam[16], F. Andrade-Oliveira[17], J. Annis[16], J. Asorey[18], E. Bertin[19,20], S. Bocquet[21], D. Brooks[22], D. L. Burke[23,24], A. Carnero Rosell[15,25,26], D. Carollo[27], M. Carrasco Kind[28,29], J. Carretero[30], M. Costanzi[27,31,32], L. N. da Costa[15], M. E. S. Pereira[33], P. Doel[22], S. Everett[34], I. Ferrero[35], B. Flaugher[16], D. Friedel[28], J. Frieman[13,16], J. García-Bellido[36], M. Gatti[37], D. W. Gerdes[17,38], K. Glazebrook[1], D. Gruen[21], J. Gschwend[15,39], G. Gutierrez[16], S. R. Hinton[9], D. L. Hollowood[40], K. Honscheid[41,42], D. Huterer[17], D. J. James[6], K. Kuehn[43,44], N. Kuropatkin[16], U. Malik[3], M. March[37], F. Menanteau[28,29], R. Miquel[30,45], R. Morgan[46], B. Nichol[47], R. L. C. Ogando[39], A. Palmese[48], F. Paz-Chinchón[28,49], A. Pieres[15,39], A. A. Plazas Malagón[50], M. Rodriguez-Monroy[18], A. K. Romer[51], E. Sanchez[18], V. Scarpine[16], I. Sevilla-Noarbe[18], M. Soares-Santos[17], E. Suchyta[52], G. Tarle[17], C. To[41], B. E. Tucker[3], D. L. Tucker[16], T. N. Varga[53,54,55]

ABSTRACT

We use stacked spectra of the host galaxies of photometrically identified type Ia supernovae (SNe Ia) from the Dark Energy Survey (DES) to search for correlations between Hubble diagram residuals and the spectral properties of the host galaxies. Utilising full spectrum fitting techniques on stacked spectra binned by Hubble residual, we find no evidence for trends between Hubble residuals and properties of the host galaxies that rely on spectral absorption features ($< 1.3\sigma$), such as stellar population age, metallicity, and mass-to-light ratio. However, we find significant trends between the Hubble residuals and the strengths of [OII] (4.4σ) and the Balmer emission lines (3σ). These trends are weaker than the well known trend between Hubble residuals and host galaxy stellar mass (7.2σ) that is derived from broad band photometry. After light curve corrections, we see fainter SNe Ia residing in galaxies with larger line strengths. We also find a trend (3σ) between Hubble residual and the Balmer decrement (a measure of reddening by dust) using Hβ and Hγ. The trend, quantified by correlation coefficients, is slightly more significant in the redder SNe Ia, suggesting that bluer SNe Ia are relatively unaffected by dust in the interstellar medium of the host and that dust contributes to current Hubble diagram scatter impacting the measurement of cosmological parameters.

Key words: galaxies: general - transients: supernovae - cosmology: observations - surveys

1 INTRODUCTION

Standardised Type Ia supernovae (SNe Ia) are important distance indicators used to probe the expansion history of the universe (Riess et al. 1998; Perlmutter et al. 1999) and measure the local Hubble constant (H_0) (Dhawan et al. 2020; Khetan et al. 2021; Freedman 2021; Riess et al. 2021). SNe Ia are extremely bright stellar explosions with a peak magnitude in the B-band of ~ -19.5 mag (Childress et al. 2017). They are standardised through light curve corrections that account for the relationship between the peak magnitude and the stretch or width of the SN Ia light curve (Phillips 1993)

and the relationship between the peak magnitude and SN Ia colour (Tripp 1998).

Many studies over the last two decades have further improved the standardisation of SNe Ia by making use of broad band photometry and spectroscopy of host galaxies to correct for trends between the colour and stretch corrected luminosities of SNe Ia and the properties of the host. These include gas phase metallicity (D'Andrea et al. 2011; Pan et al. 2014), stellar age (Childress et al. 2013; Rose et al. 2019), specific star-formation rate (Lampeitl et al. 2010; D'Andrea et al. 2011; Childress et al. 2013; Rigault et al. 2020) and rest-frame colour (Roman et al. 2018; Kelsey et al. 2021; Kelsey

et al. 2022). The most commonly used correction is with the stellar mass of the host galaxy. The correction is applied as a step function around $10^{10} M_\odot$, and is referred to in the literature as the "mass step" where SNe Ia in high mass galaxies ($> 10^{10} M_\odot$) are more luminous after correction than SNe Ia in low mass galaxies (Kelly et al. 2010; Sullivan et al. 2010; Guy et al. 2010; Childress et al. 2013; Uddin et al. 2017; Smith et al. 2020b; Kelsey et al. 2021).

The mass step has been found with varying significance. A mass step of 0.039 ± 0.016 mag was uncovered using the Pantheon sample (Scolnic et al. 2018), while Brout et al. (2019b) found no evidence of a mass step (0.009 ± 0.018 mag), when using SNe Ia from the Dark Energy Survey (DES). However, Smith et al. (2020b) observed a significant mass step of 0.040 ± 0.019 mag when utilising the same sample, and showed that the magnitude of the mass step was affected by the way survey selection biases were computed. The size of the mass step also depends on the method used to standardise SN Ia luminosities. Boone et al. (2021) find a mass step of 0.092 ± 0.026 mag using their SN Ia sample and the SALT2 standardisation method (Betoule et al. 2014), and a reduced step of 0.040 ± 0.020 mag when using an alternative standardisation method (Twin Embedding Model).

The relationship between SN color and peak brightness is modelled with a single term in the Tripp equation (Tripp 1998). However, it is likely that there are a least two mechanisms at play: an intrinsic relation between luminosity and color and reddening and attenuation by dust. There is no reason why these two mechanisms should follow the same relationship. Attenuation by dust is wavelength dependent and is defined by an attenuation law. The law depends on the dust grain size and composition, and varies within the Milky Way and from galaxy to galaxy. It has been found to correlate with host galaxy properties. For example, high mass galaxies tend to have greater attenuation in the V-band and shallower attenuation laws[1], when compared with low mass galaxies (Salim et al. 2018).

In a recent work, Brout & Scolnic (2021) found that the mass step could be reproduced in a model that allowed the attenuation law and the amount of attenuation to vary with host galaxy mass. Furthermore, the observed trends in Hubble residuals and SN color were well captured by a model (hereafter referred to as the BS21 model) which combined an intrinsic SN colour-magnitude relation with attenuation laws that depended on host galaxy mass. Independently, Johansson et al. (2021) recovered a significant mass step when assuming a fixed attenuation law with $R_V = 2$. However, when utilising an individual best fit value of R_V for each SN Ia, the mass step vanished. Additionally, Meldorf et al. (2022) find agreement between the fitted colour slope from the SN Ia photometry and fitted host galaxy R_V from host photometry when splitting the sample on galaxy population.

The goal of our work is to search for correlations between Hubble residuals and SN Ia host galaxy properties. Instead of deriving host galaxy properties from broad band photometry as most studies have done (e.g. Sullivan et al. 2010; Rigault et al. 2013; Uddin et al. 2017; Rose et al. 2019; Smith et al.

2020b; Kelsey et al. 2021; Johansson et al. 2021), we use spectra. Spectra offer the possibility of capturing trends that cannot be extracted using photometry. Using spectra from the Sloan Digital Sky Survey (SDSS), Johansson et al. (2013) find no significant trends between properties measured from spectra and Hubble residuals. Using a larger sample of SDSS SNe Ia, Campbell et al. (2016) find a weak trend between Hubble residuals and galaxy metallicity, while Galbany et al. (2022) recently found trends between Hubble residuals with metallicity, specific-star formation rate and the equivalent width of Hα.

The sections of this paper consist of the following: In Section 2, we describe the SN Ia sample used in the analysis. In Section 3, we describe the spectral fitting technique that is used to extract galaxy properties from stacked host galaxy spectra. Then, in Section 4 we search for trends between Hubble residuals and these properties. Section 5 discusses the results.

2 SURVEYS AND DATA SELECTION

2.1 The Dark Energy Survey (DES)

The Dark Energy Survey (DES) was designed to constrain the properties of dark energy using four probes: galaxy clusters, weak lensing, Baryon Acoustic Oscillations, and SNe Ia (DES Collaboration et al. 2016). Running for six observing seasons, from 2013 to 2019, and using the 570 megapixel Dark Energy Camera (DECam; Flaugher et al. 2015) mounted on the 4-m Victor M. Blanco Telescope (DES Collaboration et al. 2016), DES consists of two surveys: a wide survey covering 5100 square degrees; and a 27 square degree time domain survey covering 10 deep fields with weekly cadence in the griz bands. DES has catalogued hundreds of millions of galaxies and has discovered thousands of supernovae (Hartley et al. 2022). The data is passed through the DES Image Processing Pipeline (Morganson et al. 2018), where transients are identified using a difference imaging pipeline (Brout et al. 2019a).

2.2 The Australian Dark Energy Survey (OzDES)

The Australian Dark Energy Survey (OzDES) was undertaken over the same six observing seasons as DES (Yuan et al. 2015; Childress et al. 2017; Lidman et al. 2020). Observations were performed on the 3.9-m Anglo-Australian Telescope (AAT) at Siding Spring Observatory and utilised the AAOmega spectrograph with the 2dF field positioner (Yuan et al. 2015) to target the 10 deep fields that are a part of the DES time domain survey. The 2dF fibre positioner can place up to 8 guide fibres and 392 science fibres within a 2.1 degree field, matching the field of view of the DECam imager. Its primary aims were measuring redshifts of SN hosts, confirming the spectral type of SNe, and monitoring AGNs over a wide range of redshift (Hoormann et al. 2019). OzDES spectra have previously been used in a number of studies (Wiseman et al. 2020b; Pursiainen et al. 2020; Smith et al. 2020a). The faintest objects have an apparent magnitude $r \approx 24$ mag and the wavelength coverage is between 3700 and 8800Å. The second OzDES data release includes 375,000 spectra of 39,000 objects. A full description of the data can be found in Lidman et al. (2020).

---

[1] Attenuation laws are often parameterised with R_V, the total to selective extinction ratio. Shallower attenuation laws have higher R_V values.

Table 1. The size of the sample after each cut is applied.

Cut	Number of SNe Ia
SN Ia Photometric Sample	1484
Matching SN transient with a host galaxy with an OzDES observation	1181
Redshift reliability $> 95\%$	874
OzDES spectra not contaminated by SN light	625

2.3 Type Ia Supernovae Sample

We utilise the DES5YR-SN photometric sample described in Möller et al. (2022). The SNe Ia were classified with the SuperNNova (SNN) classifier (Möller & de Boissière 2020). SNN identifies SNe Ia with high accuracy and high purity. The sample contains 1484 photometrically classified SNe Ia, and includes light curve quality cuts for the colour (c) and stretch ($x1$): $-0.3 < c < 0.3, -3 < x1 < 3$ (Betoule et al. 2014).

We then implement specific cuts (Table 1). For each DES transient, the host is identified as the galaxy with the smallest directional light radius (DLR; Gupta et al. 2016) from the deep image stacks described in Wiseman et al. (2020a). We then match the host with objects in the OzDES redshift catalogue (Lidman et al. 2020), and a cut is made regarding the quality of the spectroscopic redshift. The OzDES redshift reliability criterion is determined by the quality of the matched spectroscopic features. A flag $= 3$ redshift is based on identifying a single strong spectroscopic feature or multiple weak features, and is likely to be correct more than 95% of the time. Redshifts with a flag $= 4$ are based on multiple strong features and are likely to be correct more than 99% of the time. We require the quality flag ≥ 3 in our analysis, and omit any galaxies without a spectroscopic redshift.

We also only use spectra of the hosts that are not contaminated by supernova light. For this reason we select OzDES host galaxies that were observed two months before or five months after the SN Ia peak luminosity occurred. Around maximum brightness, light from the SN can contaminate and potentially bias the spectrum of the host. These cuts reduce the number of SNe Ia in our sample from 1484 to 625.

3 METHODOLOGY

3.1 Hubble Residuals

Hubble residuals ($\Delta\mu$) are the deviation between the inferred distance modulus (μ_{obs}) and the expected value at a given redshift and cosmological model ($\mu_{\mathrm{theory}}(z)$):

$$\Delta\mu = \mu_{\mathrm{obs}} - \mu_{\mathrm{theory}}(z). \tag{1}$$

A positive (negative) Hubble residual implies that the SN is fainter (brighter) than the model. Each SN Ia light curve is fit using the SALT2 light curve model (Guy et al. 2010) that was trained for the Joint Light Curve Analysis (Betoule et al. 2014). This fit gives a colour (c), stretch (x_1), and apparent magnitude at peak brightness in the B-band (m_B). These parameters are then used to estimate the distance modulus (μ_{obs}), by applying the modified Tripp formula (Tripp 1998):
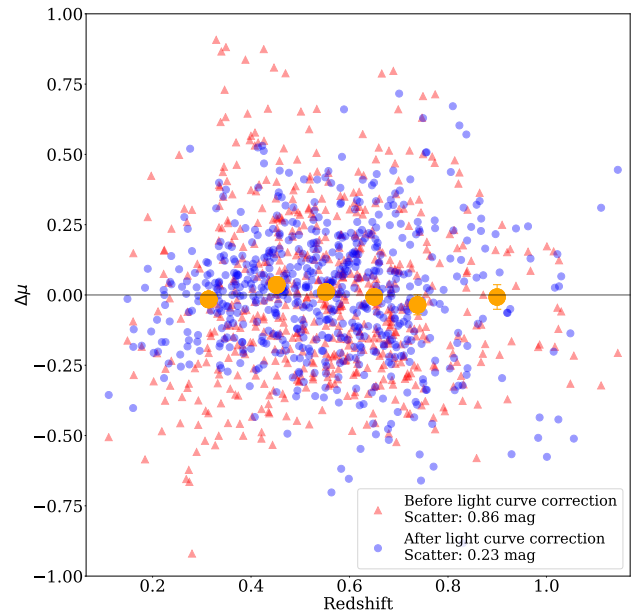

Figure 1. Hubble residual diagram for the OzDES SN Ia host galaxy sample containing 625 SNe Ia. The red points are the residuals before light curve correction and the blue points have been corrected for colour, stretch and survey selection biases. The median redshift of the sample is $z \sim 0.55$. Mean scatter of the residuals split into redshift bins are shown as the orange points.

$$\mu_{\mathrm{obs}} = m_{\mathrm{B}} + \alpha x_1 - \beta c + M_0 + \gamma G_{host} + \mu_{bias}. \tag{2}$$

The nuisance parameters (α, β) are set to $\alpha = 0.156 \pm 0.012$ and $\beta = 3.201 \pm 0.131$ (Smith et al. 2020b) and the absolute magnitude is set to $M_0 = -19.5$. The bias correction term, μ_{bias}, is obtained from simulations using BBC (Kessler & Scolnic 2017) and takes into account survey selection effects.

The term γG_{host} is the correction for the mass step and is usually formulated as:

$$G_{\mathrm{host}} = \begin{cases} +1/2 & \text{for } M_* > M_{\mathrm{step}} \\ -1/2 & \text{otherwise,} \end{cases} \tag{3}$$

where M_* is the stellar mass of the SN host galaxy, and γ is the size of the mass step. The division point (M_{step}) is generally taken as 10^{10} $\mathrm{M}_\odot$.

We exclude the mass step term (γG_{host}) and use a 1D bias correction (Smith et al. 2020b) in our analysis. This allows us to investigate the significance of any dependencies between Hubble residuals and host galaxy properties in our sample.

Figure 1 shows the Hubble residual diagram with the 625 SNe Ia remaining after the cuts to the DES5YR photometrically selected SN Ia sample. For each SN Ia we plot $\Delta\mu$ and then apply the light curve and 1D bias corrections. The scatter reduces from 0.86 to 0.23 mag after these corrections.

Figure 2 shows the trend between host stellar mass and Hubble residual. We make use of masses obtained using the method described in Smith et al. (2020b), which were estimated using broadband photometry of the host galaxies in the deep image stacks of the DES-SN fields (Wiseman et al. 2020a). The trend is fitted with a straight line, and as seen in other large SN surveys, the more luminous SNe Ia after light curve correction (negative residuals) reside in galaxies
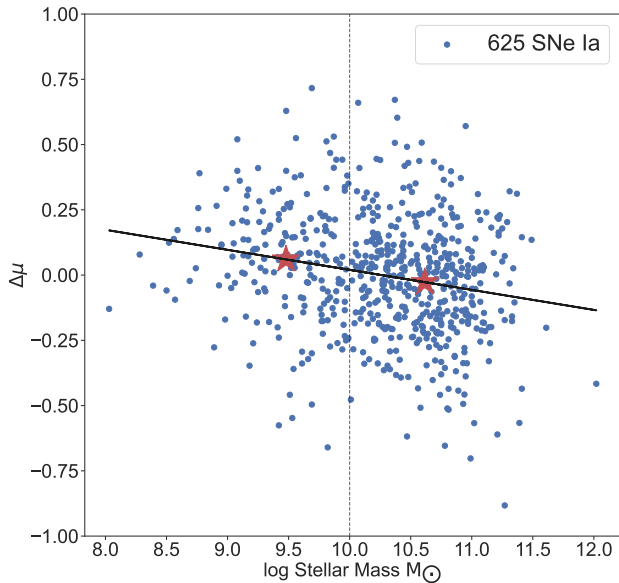
Figure 2. The DES5YR photometrically selected SN Ia sample after selection cuts (Table 1), standard light curve corrections ($\alpha = 0.156$ and $\beta = 3.201$) and 1D bias corrections, showing Hubble residual against host galaxy stellar mass. The black line corresponds to a linear fit and the red stars are the average Hubble residual either side of $10^{10} M_{\odot}$. The linear fit has a slope -0.087 ± 0.014 and the mass step between the averaged points is 0.087 ± 0.011, which is comparable to that found for DES3YR SN Ia sample. (Smith et al. 2020b).

with higher stellar masses. The median stellar mass of the host galaxies is $10^{10.34} M_{\odot}$, so there are more galaxies with masses above $10^{10} M_{\odot}$, the canonical mass used for the mass step, than below it.

3.2 Coadding and Stacking OzDES Host Galaxy Spectra

In this work we use the term coadding when combining spectra of the same object and stacking when combining spectra of different objects.

3.2.1 Coadded OzDES Spectra

The SN host galaxies in our sample cover a broad range of apparent magnitude, between $18 < r < 24$. Integration times for the faintest hosts were very long (up to 100 hours in some cases), and most targets were observed over several nights. During this time, the seeing and transparency can vary greatly, which results in large fluctuations in the amount of light entering the fibres. Consequently, the throughput varied by an order of magnitude. To overcome this variability, the OzDES data reduction pipeline scales the data with the inverse of the median flux of the extracted spectrum.[2] The

---

[2] In detail, the pipeline scales each spectrum with either the median of the flux or 0.1 times the square root of the median variance, whichever is greater. The scaling is computed from data obtained in the red arm of AAOmega and is applied to both the red and blue arms.

variance spectrum is scaled by the square of this scaling factor. The coadded spectrum is the variance weighted average of the scaled spectra. By design, the continuum of the red half of the coadded spectrum has a median that is close to one.

3.2.2 Stacking OzDES Spectra

Due to the low signal-to-noise ratio (S/N) of coadded spectra, we split the SN Ia host galaxies into stacks based on the size of the Hubble residual and compute the variance-weighted average spectrum for each stack. The first step is to deredshift each spectrum. This is done using linear interpolation to a common wavelength grid.

The spectra are stacked using the same procedure as that used for the individual spectra. Again, the stacked spectra have a median that is close to one, as can be seen in Figure 3.

To understand how uncertainties affect our analysis, we implement two approaches. We capture the formal variance by perturbing each point in the averaged spectrum. The magnitude of the perturbation is drawn from a Gaussian that has a mean of zero and a variance that is determined from the variance spectrum. This is repeated 1000 times. However, the formal variance does not capture the intrinsic variability of the individual spectra. To capture the intrinsic scatter we perform 1000 bootstrap samples of the spectra used in the stack.

The method of coadding and stacking spectra has a number of consequences. The integrated line fluxes are scaled relative to the continuum between 5700Å and 8600Å, so line fluxes are not absolute. Instead, they can be better described as continuum normalised fluxes, which we simply refer to as line strengths throughout this paper. Line flux ratios are unchanged as the same scaling is applied to all lines. Equivalent widths are also unchanged as the same scaling is applied to both the continuum and the line.

3.2.3 Systematic uncertainties in the calibration of OzDES data

The conversion from counts measured on the detector to spectral flux densities requires two sensitivity curves, one for each arm of the AAOmega spectrograph. To determine these curves, OzDES allocated 8 to 12 fibres to F stars in every configuration. These stars were observed at the same time as the galaxies. In principle, OzDES could have produced sensitivity curves for every observation, but chose instead to use curves that were determined using data obtained during the first two OzDES observing seasons.

When done in this way, the spectral flux densities are relative and not absolute, as flux losses caused by the finite area of the fibres are not taken into account. Additionally, other errors can lead to chromatic warping of the spectra. These errors include field and wavelength dependent aberrations from the 2dF corrector, errors in the positioning of the fibres, and variations in the natural seeing. As demonstrated in Hoormann et al. (2019), the warping of the spectra can be removed by applying a second order polynomial that is derived from the comparison of broad band photometry of the objects with synthetic photometry derived from the
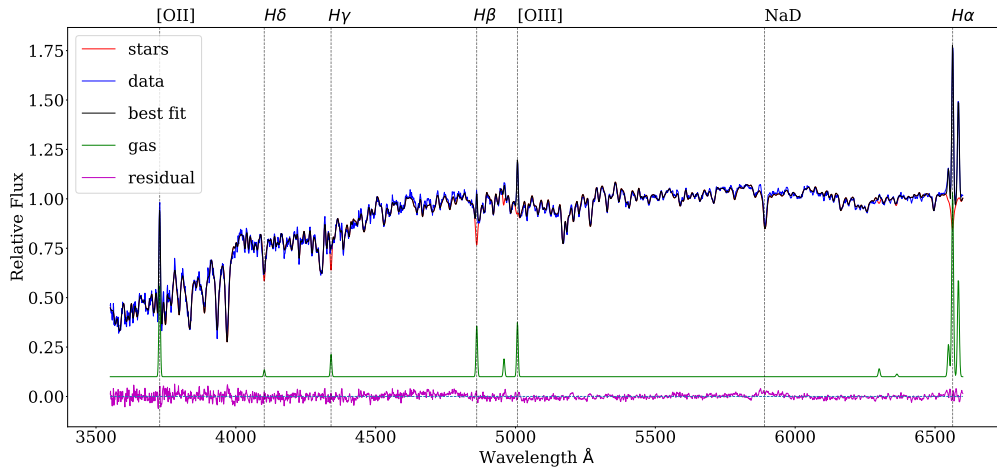
Figure 3. An example of running pPXF on a OzDES host galaxy stack (76 objects with $z \leq 0.35$). The blue line represents the input spectrum, the black line is the best fit, the red and green lines (the latter shifted up 0.1 for clarity) are the stellar and emission line components, respectively, and the purple line is the residual flux. Note how the Balmer emission lines fill in the absorption lines from the stars.

Table 2. pPXF output for each of the stacked spectra, where the uncertainties were obtained using bootstrap resampling.

$\Delta\mu$	log Stellar Age (yrs)	Mass-to-light ratio	Metallicity [M/H]	Equivalent Width [OII] (Å)	log Stellar Mass $M_\odot$
-0.37	9.68 ± 0.07	2.12 ± 0.22	-0.13 ± 0.02	-5.81 ± 0.73	10.46 ± 0.09
-0.23	9.79 ± 0.07	2.47 ± 0.35	-0.2 ± 0.04	-6.26 ± 1.03	10.53 ± 0.06
-0.17	9.8 ± 0.07	2.53 ± 0.36	-0.2 ± 0.04	-5.78 ± 1.23	10.40 ± 0.09
-0.12	9.88 ± 0.09	2.95 ± 0.65	-0.24 ± 0.07	-6.69 ± 2.38	10.31 ± 0.09
-0.06	9.83 ± 0.05	2.35 ± 0.24	-0.51 ± 0.12	-8.46 ± 1.24	10.26 ± 0.09
-0.01	9.73 ± 0.09	2.10 ± 0.30	-0.23 ± 0.06	-7.2 ± 1.35	10.27 ± 0.09
0.02	9.87 ± 0.05	2.87 ± 0.39	-0.21 ± 0.03	-8.7 ± 1.74	10.35 ± 0.09
0.06	9.81 ± 0.08	2.13 ± 0.32	-0.47 ± 0.17	-14.38 ± 1.5	10.09 ± 0.08
0.10	9.48 ± 0.18	1.45 ± 0.34	-0.13 ± 0.09	-10.53 ± 1.84	10.02 ± 0.10
0.16	9.68 ± 0.11	1.88 ± 0.50	-0.42 ± 0.2	-9.21 ± 2.72	10.12 ± 0.11
0.23	9.89 ± 0.05	2.79 ± 0.34	-0.33 ± 0.15	-9.38 ± 2.29	10.09 ± 0.10
0.39	9.81 ± 0.05	2.47 ± 0.28	-0.18 ± 0.02	-10.66 ± 2.11	10.02 ± 0.09

flux calibrated spectra. This works well for relatively bright sources, but works less well for sources considered here, many of which are considerably fainter than the sky. For such objects, a small error in the subtraction of sky can lead to a big impact on the continuum and to an erroneous estimate of the amount of warping required.

Hence, the spectra used in this work are stacked without warping. The systematic error associated with neglecting the correction is small and can be estimated from the F stars themselves. As noted above, about a dozen F stars are allocated fibres and observed at the same time as the supernovae host galaxies. Over the 6 years OzDES ran, nearly 10,000 F star spectra were obtained. We use these spectra to estimate how much tilt needs to be applied so that the observed and modeled spectra of the the F stars agree. We find a scatter of 24% per 100 nm for the tilt in the blue arm and a scatter of 7% per 100 nm for the tilt in the red arm. The scatter is for a single observation. The stacked host galaxy spectra consist of spectra from around 100 host galaxies that are randomly distributed across the 2dF field. Under the assumption that the tilts are also randomly distributed, the tilt in the stacked spectra will be lower, by approximately the tilt in the spectrum of a single galaxy divided by the square root of the

number of galaxies. The tilt in the combined spectra is expected to be of the order of a few percent per 100 nm. It is considerably smaller than the statistical uncertainties and hence is not included in our analysis.

3.3 Spectral Fitting

Penalized Pixel-Fitting (pPXF) is used to extract information on the stellar population from our stacked galaxy spectra. pPXF is a full spectrum fitting technique which utilises a penalised maximum-likelihood approach (Cappellari & Emsellem 2004). pPXF is one option that is widely used and trusted in its full spectral fitting implementation. While other useful tools such as Prospector (Johnson et al. 2021) could be utilised, we find the excellence of the fit provided by pPXF sufficient for our approach in deriving host properties to search for trends with Hubble residual.

A single stellar population (SSP) model consists of groups of stars with the same metallicity, a given IMF and all formed at the same time. A general stellar population is then a linear combination of SSPs. The MILES spectral library is used to build the synthetic spectrum, ranging in age from 0.63 to 17.8 Gyr and metallicity from -2.32 to 0.22 [M/H] with a
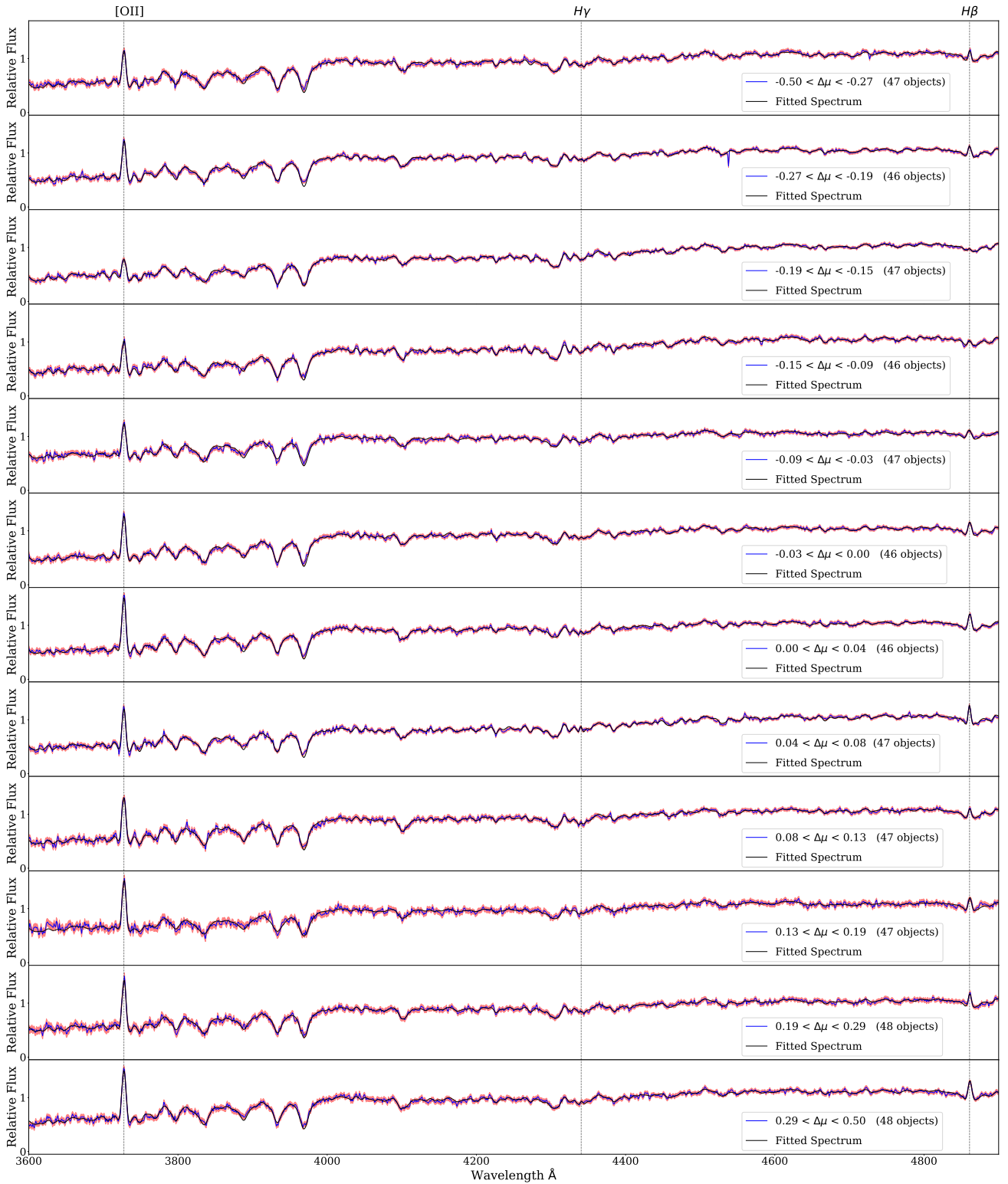
Figure 4. Stacked OzDES spectra which are binned by Hubble residual for $z \leq 0.8$. Each stack contains a similar number of objects, resulting in high S/N. The blue line represents the data while the black line is the fit obtained using pPXF. The filled red area indicates the standard deviation obtained from bootstrap resampling.
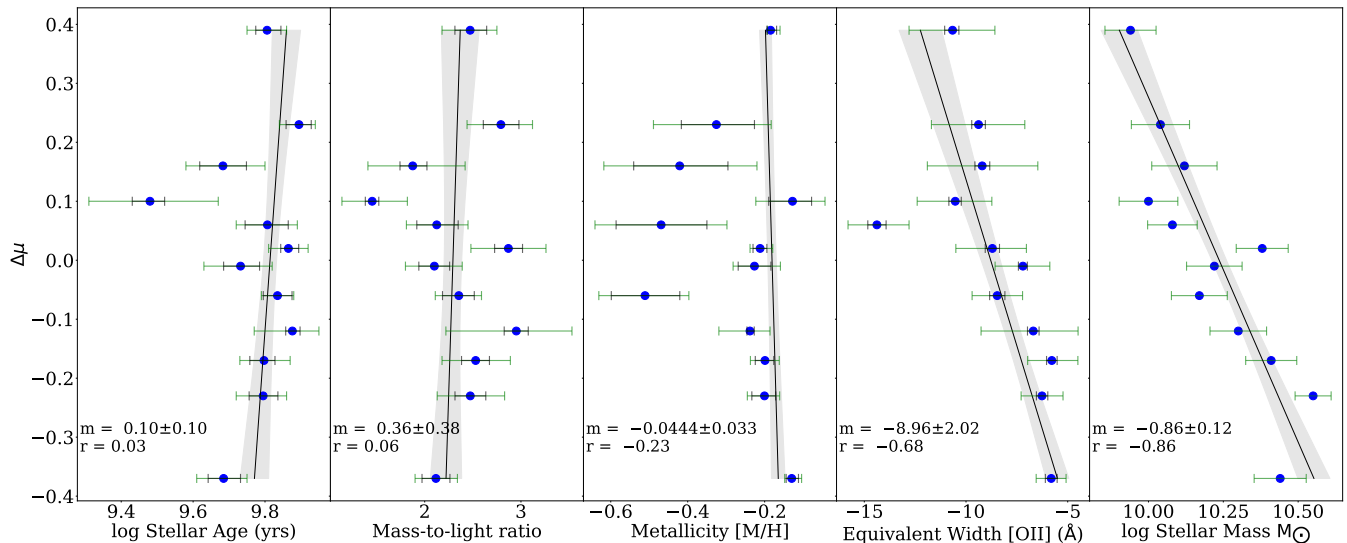
Figure 5. Left to right: Trends between host galaxy properties and Hubble residuals. The first four plots are derived using spectra, while the last plot is derived using photometry. The outer green errorbars are computed by bootstrap resampling and the inner black errorbars are obtained from the formal variance. We show a linear fit for each property, with 1σ confidence intervals. m represents the slope. The trend between host stellar mass and Hubble residual is the most significant and has the highest Pearson correlation coefficient, r.
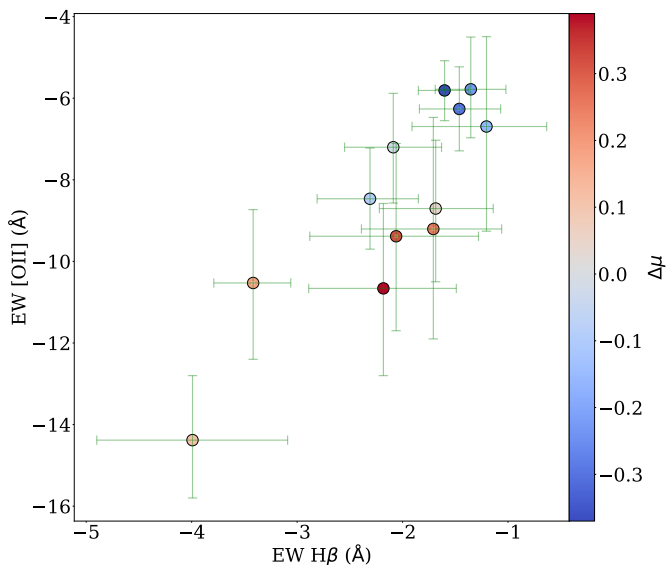
Figure 6. A plot comparing the EWs of [OII] and Hβ. Note how the EWs of both lines correlate with Hubble residual. Hosts with the strongest emission lines (more negative EWs) also tend to host SN Ia with positive Hubble residuals (colour bar).

unimodal IMF with a slope of 1.30 (Vazdekis et al. 2010). They were obtained at the 2.5-m Isaac Newton Telescope (INT) in Spain over the wavelength range 3525-7500 Å at a resolution of 2.5 Å, which is well suited to the wavelength range covered by the OzDES spectra. The full approach is described by Cappellari (2017).

We run the stacked spectra through pPXF to extract information about the stellar population. Figure 3 shows the resulting high quality fit obtained using pPXF on an example OzDES stack. The output consists of the relative flux of the input spectrum, the best fit from the stellar templates, gas emission lines, and fit residuals. We also obtain weighted ages, metallicities and mean mass-to-light ratios of the best fit stellar population. We note that an individual OzDES spectrum is not suited for using full spectrum fitting due to the low S/N of individual spectra.

4 RESULTS

4.1 Trends between Hubble residual and host properties

Here we explore trends between Hubble residuals and the properties of the hosts derived from DES photometry and OzDES spectroscopy. We apply a redshift cut ($z \leq 0.8$), and then split the sample into 12 bins between $-0.50 < \Delta\mu < 0.50$, with a similar number of objects per bin. The bin size is chosen so that the S/N of the stacked spectra is sufficient for a reliable pPXF fit (Figure 4).

pPXF fits for both the continuum that comes from stars and nebula emission lines from the ISM. As the spectra are normalised by the continuum before stacking, the line fluxes cannot be transformed into star formation rates. Instead, the line fluxes are more closely related to the specific star formation rate (sSFR); see Section 3.2 for a discussion on how the OzDES data are scaled before coadding and stacking.

In Figure 5, we plot each of the host galaxy properties obtained from pPXF fits to the stacked spectra against Hubble residuals. We also show the average stellar mass for each stack obtained from the photometry. The outer errorbars for each point were obtained from bootstrap resampling, with the 1σ confidence intervals reported in Table 2. Given that these errors are small ($\lesssim 0.01$ mag), they can be safely ignored. We fit a linear relation to each property instead of a step function to better capture the trends in our data, the results of which are summarized in Table 3.

The host stellar mass trend is the most significant, although interestingly no trend is present in the mass-to-light ratio,

Table 3. For each of the galaxy properties we show the slope of the best straight line fit, significance and the Pearson correlation coefficient, to give an indication of the strength of any trend. The most significant trend is between stellar mass and Hubble residual. The trend between the strength of the [OII] line and Hubble residual is the next most significant. The remaining properties show no obvious trends.

Host Property	Slope	Significance (σ)	Correlation
log Stellar Age (yrs)	-0.10 ± 0.10	0.99	0.03
Mass-to-light ratio	-0.25 ± 0.35	0.95	0.06
Metallicity [M/H]	-0.044 ± 0.033	1.33	-0.23
Equivalent Width [OII] (Å)	-8.96 ± 2.02	4.44	-0.68
log Stellar Mass $M_\odot$	-0.86 ± 0.12	7.2	-0.88
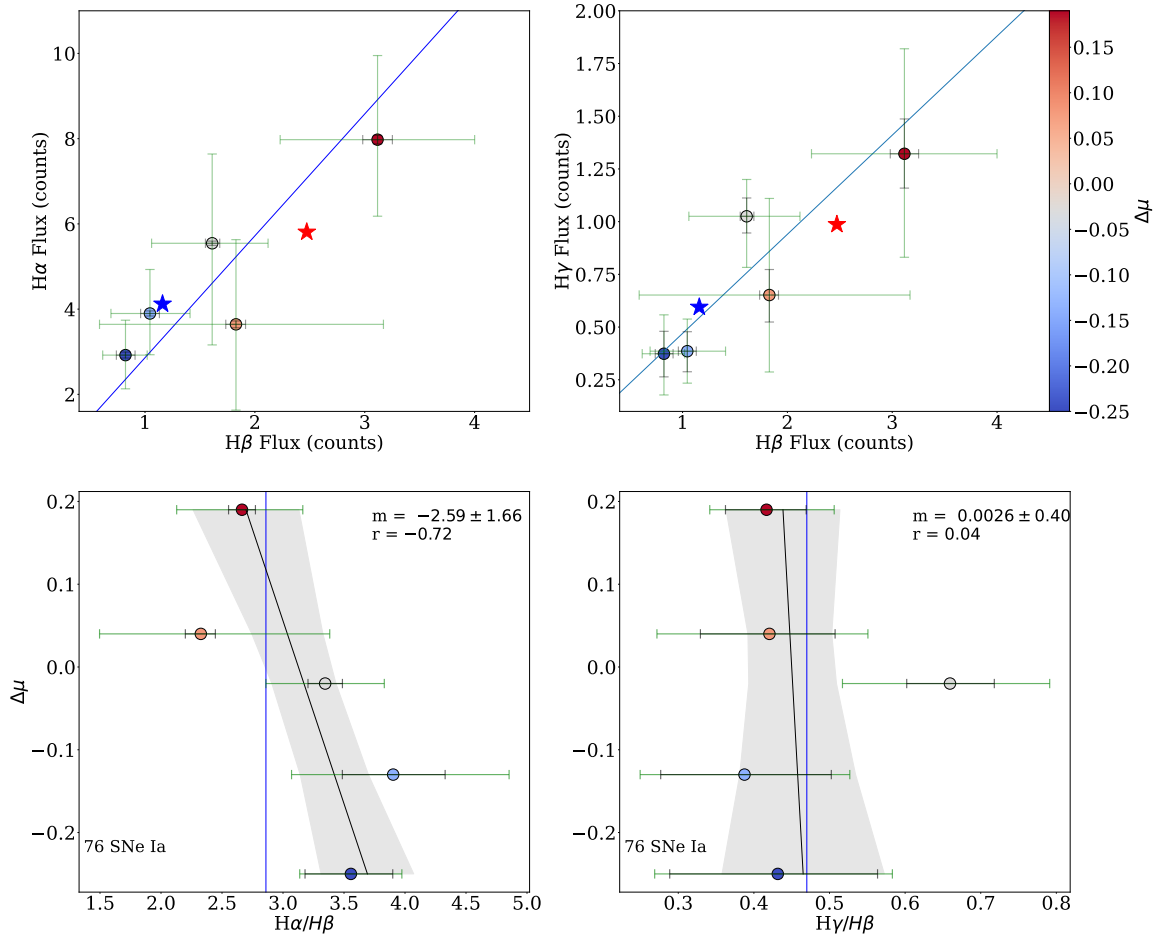
Figure 7. Top: The ratio of emission line strengths for the low redshift sample, $z \leq 0.35$, with the blue line corresponding to the theoretical Balmer ratio in each case. The Balmer lines tend to be stronger for the fainter SNe Ia. The red/blue stars show the mean line strengths for the positive/negative Hubble residuals. Bottom: Balmer ratio against Hubble residual for the same sample of SN Ia hosts. We see a possible trend between Hubble residual and Hα/Hβ with a slope of -2.59 ± 1.66 and $r = -0.72^{-0.15}_{+0.22}$ and no trend for Hγ/Hβ with a slope of -0.00 ± 0.40, and $r = 0.04^{+0.37}_{-0.34}$.

suggesting the correlation may not be heavily influenced by the stellar populations themselves. Rather than a sharp transition at a single mass, we see a gradual trend.

From the OzDES galaxy spectra, [OII] shows the clearest trend, with the positive residuals residing in galaxies with larger [OII] line fluxes and therefore with higher sSFRs. As noted above, the spectra are normalised by the continuum before stacking, so line fluxes are more closely related to the specific star formation rate (sSFR) than the absolute SFR.

In Figure 6, we plot the EW of [OII] against the EW of $H\beta$, finding a clear correlation between the two lines. As both lines are sensitive to star formation, the EWs are a measure of the sSFR, and the correlation between the two EWs is expected. Note how the EWs of both lines correlate with Hubble residual. Hosts with large EWs and therefore larger specific star formation rates also tend to host SN Ia with more positive Hubble residuals.

The trend between Hubble residual and the sSFR has been

Table 4. Similar to Table 2, containing the mean values and resulting errorbars from Figure 8.

$\Delta\mu$	$H\gamma$	$H\beta$	Balmer Ratio ($H\gamma/H\beta$)
-0.37	0.76 ± 0.12	1.36 ± 0.18	0.56 ± 0.07
-0.23	0.63 ± 0.17	1.19 ± 0.31	0.53 ± 0.07
-0.17	0.50 ± 0.15	1.10 ± 0.26	0.45 ± 0.07
-0.12	0.51 ± 0.21	1.03 ± 0.52	0.52 ± 0.12
-0.06	0.87 ± 0.24	1.86 ± 0.34	0.47 ± 0.08
-0.01	0.90 ± 0.20	1.63 ± 0.36	0.56 ± 0.07
0.02	0.60 ± 0.16	1.38 ± 0.45	0.45 ± 0.07
0.06	1.29 ± 0.21	3.15 ± 0.71	0.42 ± 0.06
0.10	1.45 ± 0.17	2.68 ± 0.28	0.54 ± 0.04
0.16	0.58 ± 0.25	1.42 ± 0.58	0.41 ± 0.10
0.23	0.67 ± 0.27	1.76 ± 0.64	0.37 ± 0.07
0.39	0.70 ± 0.28	1.88 ± 0.59	0.37 ± 0.08

seen in previous studies (Sullivan et al. 2010; Galbany et al. 2022) and found to be the strongest step when using local sSFR (Rigault et al. 2020; Briday et al. 2022). Lastly we find no trend with stellar population age and only a weak trend with metallicity (Campbell et al. 2016), where metal poor host galaxies contain more positive residuals (Childress et al. 2013).

4.2 Dust

To further investigate these trends, we also probe the effect that extrinsic factors such as dust may have on the luminosity of SNe Ia after standard corrections have been applied.

A diagnostic measure of reddening due to dust is the Balmer decrement, representing the ratio between hydrogen nebular emission lines (Hα, Hβ and Hγ, etc) (Domínguez et al. 2013). For Case B recombination Hα/Hβ = 2.86 and Hγ/Hβ = 0.468 (Osterbrock 1989). Interstellar dust attenuation significantly impacts ultraviolet and visible wavelengths more than longer wavelengths. The amount of reddening can be determined by comparing the observed and theoretical Balmer decrements and any deviation will give an indication of the amount of reddening and, given an attenuation law, the amount of attenuation due to dust.

4.2.1 The Balmer Decrement

The most common Balmer line ratio used to probe reddening due to dust is Hα/Hβ, where values above the theoretical ratio 2.86 indicate the degree of reddening. However, we need to limit our selection to $z \leq 0.35$ (which we define as the low redshift sample) due to Hα becoming redshifted out of the wavelength range of our spectra. This impacts the sample size of each stack, with a small number of objects to stack resulting in a lower S/N in comparison to the larger sample. Measuring the emission line for $H\gamma$, we can also make use of the second Balmer line ratio Hγ/Hβ, where values below 0.468 give an indication of the degree of reddening.

In Figure 7, we plot the strength of the Hα line against the strength of Hβ, and make a similar plot for Hγ and Hβ. In both plots, fainter SNe Ia tend to appear in galaxies with larger line strengths. This is similar to the trend seen in Figure 6. Galaxies with larger line strengths, and therefore high
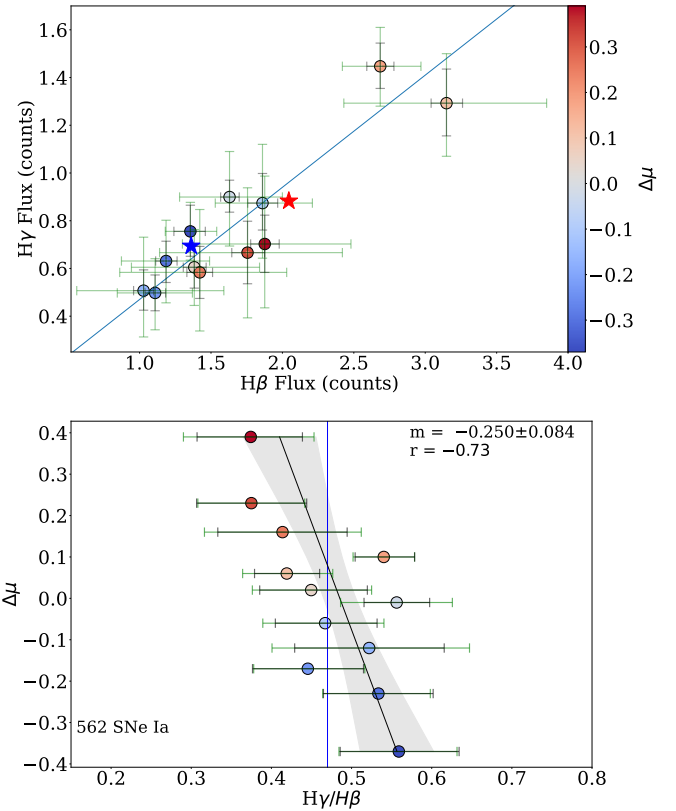

Figure 8. Top: The ratio of emission lines (Hβ and Hγ) for the sample described in Section 4, where $z \leq 0.80$. The blue line represents the expected Balmer decrement for Case B recombination of 0.468 for Hγ/Hβ. The mean line strengths for positive and negative Hubble residuals are shown as red/blue stars respectively. Below: The average Hubble residual against Balmer ratio. Similarly, the blue line corresponds to the expected value, and we observe that the hosts with more positive (fainter) Hubble residual have lower Hγ/Hβ ratios, indicating more reddening in these stacks. Fitting the data we obtain a slope of -0.176 ± 0.074, where $r = -0.52^{-0.12}_{+0.14}$.

specific star formation rates[3]. Hence the line strengths are a measure of the sSFR and not the SFR, are collectively dimmer.

In the lower panels, we plot the Hubble residual versus line ratio. If reddening is not present, then all points will lie on the vertical blue lines. We see a very weak trend with low significance between Hubble residual and the ratio of Hα and Hβ, and no trend for Hγ and Hβ. The weak trend seen using Hα and Hβ is opposite to what one expects, if dust affects both the SN Ia luminosities and the Balmer line ratio.

The Hγ and Hβ line ratio provides access to a larger sample. The increased sample size gives a more significant result. In Figure 8, the averaged trend across the stacks is that the fainter SNe Ia tend to have smaller ratios, which is consistent with the notion of attenuation and reddening by dust.

We also see the same trend between residual and line strength. Sources with more positive residuals have stronger lines and this trend is evident for all three lines. This is consis-

---

[3] When processing the OzDES data, the spectra are normalised to 1 over the observer-frame wavelength range 5800Å to 8600Å
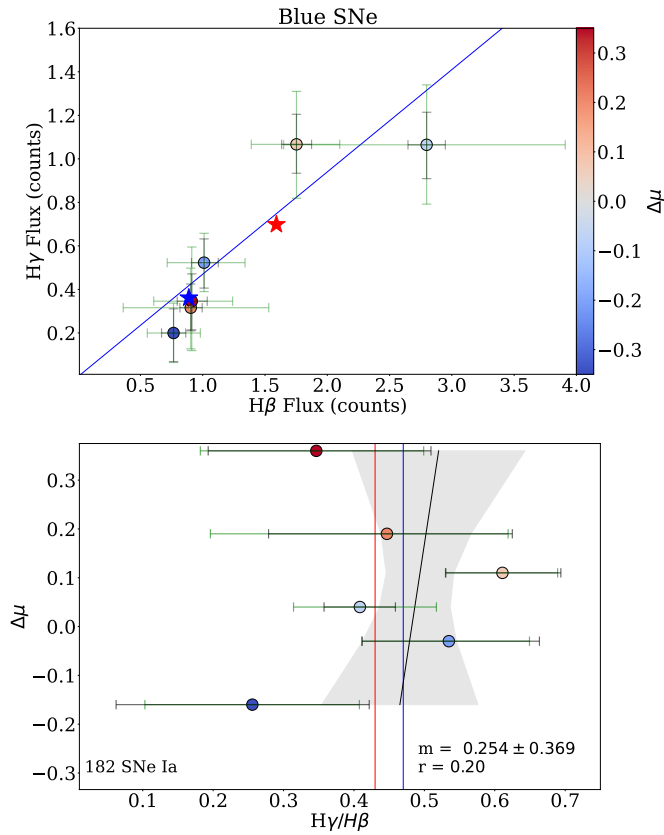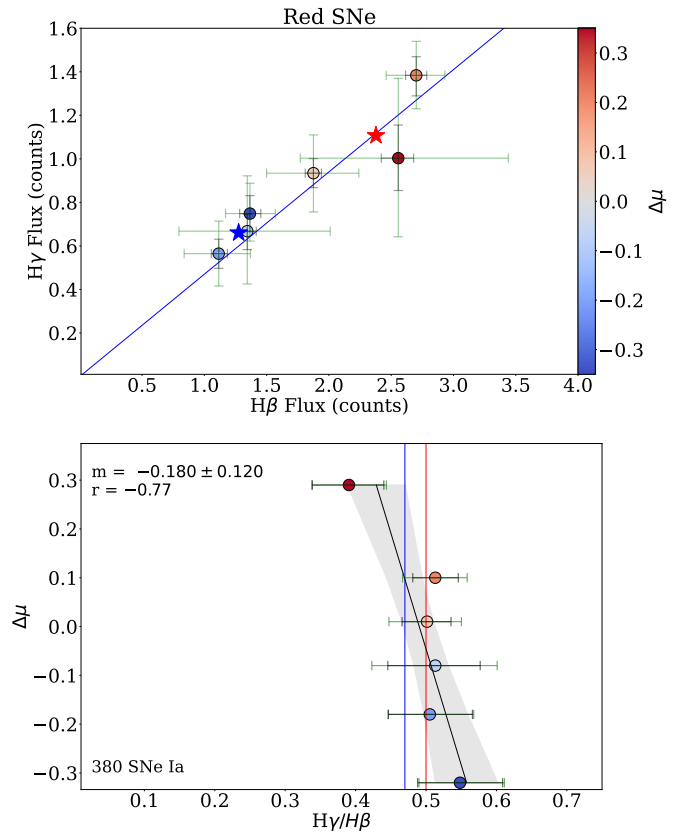
Figure 9. Host galaxy sample for blue SNe Ia ($c < -0.025$) and then binned by Hubble residual. Fitting the data we obtain a slope of 0.254 ± 0.369, where $r = 0.20^{+0.30}_{-0.33}$. The blue line represents the theoretical Balmer ratio (Osterbrock 1989), while the average Balmer ratio, shown as the red line, is 0.43 ± 0.052. Similar to previous figures, mean line strengths for positive/negative Hubble residuals are shown as red/blue stars in the top panel.

tent with the trend between the strength of [OII] and Hubble residual shown in Figure 5, as the strengths of all four lines are related to the specific star formation rate.

We note that our observed Balmer ratio correlation with Hubble residual does not offer a reddening correction for each individual object.

4.2.2 SN Colour and Reddening

We next split our sample by SN Ia colour and then bin by Hubble residual to examine if the trends noted in the previous section depend on SN Ia colour. A cut is made at $c = -0.025$, using the same dividing line as Brout & Scolnic (2021). The results are shown in Figures 9 and 10.

There are two noteworthy trends. Firstly, the redder SNe Ia tend to reside in galaxies that have stronger line strengths compared with the bluer SNe Ia, indicating higher specific star formation rates in galaxies that host red SNe Ia. The mean line fluxes of SN Ia hosts for the blue/red samples are (0.59, 0.88) for $H\gamma$ and (1.36, 1.83) for $H\beta$.

Secondly, the trend between line ratios and Hubble residuals disappears for the blue SNe Ia and remains, albeit very weakly for red SNe Ia.

Figure 10. Host galaxy sample split into redder SNe Ia ($c > -0.025$) and then binned by Hubble residual. Fitting the data we obtain a slope -0.180 ± 0.11, where $r = -0.77^{-0.11}_{+0.19}$. The blue line represents the theoretical Balmer ratio (Osterbrock 1989), while the average Balmer ratio, shown as the red line, is 0.50 ± 0.022. Similar to previous figures, mean line strengths for positive/negative Hubble residual are shown as red/blue stars in the top panel.

5 DISCUSSION

5.1 Trends with emission line strengths

We find that there are trends between Hubble residual and the strengths of [OII], $H\gamma$, $H\beta$ and $H\alpha$ emission lines of the host galaxies. We also find trends between the EWs of [OII] and $H\beta$ with Hubble residual. SNe Ia are fainter in host galaxies that have stronger emission lines and larger EWs after the standard corrections for colour and light curve width have been applied to the SNe Ia.

The EWs of the [OII] and $H\beta$ emission lines depend on the specific star formation rate (sSFR). Although other factors, e.g. metallicity, can affect the EW of [OII], generally speaking, galaxies with larger EWs have higher sSFRs and are more actively forming stars. The line strengths of [OII] and the Balmer emission lines in the OzDES spectra also depend on the sSFR, as the OzDES spectra are normalized by the continuum before coadding and stacking.

The trend between Hubble residual and the sSFR of the host galaxy has been noted by a number of other studies (Sullivan et al. 2010; Lampeitl et al. 2010; D'Andrea et al. 2011; Childress et al. 2013; Rigault et al. 2020). It has been detected using broad band photometry and spectroscopy.

Using broad band photometry of SNe Ia from the Super-

nova Legacy Survey, Sullivan et al. (2010) find that SNe Ia in galaxies with low sSFRs are brighter after light curve correction than galaxies with high sSFRs. When modelled as a step at log(sSFR) = −9.7, the step is ∼ 0.05 mag. Using spectroscopy of SNe Ia from the Sloan Digital Sky Survey, D'Andrea et al. (2011) also find that SNe Ia are brighter in galaxies that have low sSFRs.

Due to the nature of the observations and the redshifts of the hosts, these earlier works were not sensitive to the properties of the hosts in the region immediately surrounding the SN. This also applies to the OzDES data analysed in this paper. Most OzDES galaxies subtend an angular size of an arc-second, which is smaller than the 2 arc-second diameter of the 2dF fibres. Hence OzDES spectra are not sensitive to the properties of the hosts in the region immediately surrounding the SN. Instead, OzDES and these earlier works measure global properties of the hosts.

Rigault et al. (2020), using IFU spectroscopy of the hosts of nearby SNe Ia, found a trend between Hubble residuals and the properties of host galaxies in a projected 1 kpc region surrounding the site of SNe. When modelled as a step function with the step located at log(LsSFR) = −9.7, where LsSFR is the local sSFR, they found a step of 0.163 ± 0.29 mag. This is larger than the step that is measured using host galaxy mass and is the largest step measured to date.

We do not see evidence for a trend between Hubble residuals and galaxy age. As younger galaxies tend to have higher sSFRs, the lack of a trend is surprising.

As one goes to higher redshifts, the global sSFR increases, leading to a potential evolution in the SN population. At higher redshifts, there will be a higher fraction of SNe Ia in galaxies that have sSFRs above the step. This naturally leads to the question of how this may bias the estimation of cosmological parameters, such as the Hubble constant and the dark energy equation of state parameter, a question that others have examined (Childress et al. 2013; Rigault et al. 2020; Brout et al. 2022) and a topic that we will come back to in section 5.4.

5.2 Evidence for dust

We find no evidence for a trend between the properties of the host measured from the continuum of the spectra and Hubble residuals. This includes age, which is surprising, as line strengths and EWs are a measure of the sSFR which is an indicator of age. Galaxies with high sSFR are younger than galaxies with low sSFR. Could the trend be driven by another property related to the sSFR?

The amount of dust and the properties of the dust also correlate with host galaxy properties. More massive galaxies tend to be more attenuated by dust and have shallower attenuation laws (Salim et al. 2018). Dust properties also correlate with sSFR (Orellana et al. 2017; Triani et al. 2021). Galaxies with higher sSFR have higher dust-to-stellar mass ratios.

We used the Balmer line ratios in the stacked spectra as a measure of the reddening by dust and searched for correlations between the Balmer line ratios and Hubble residuals. There is some evidence that the Hγ/Hβ line ratio correlates with Hubble residual, but the trend is not very significant. Fainter SNe Ia tend to lie in galaxies that have smaller Hγ/Hβ line ratios, consistent with the idea that the galaxies that hosted these SNe Ia are more affected by dust. The trend

appears to be driven by the redder SNe Ia. When the sample is split by SN Ia colour, the evidence for a trend persists for the red SNe Ia (defined here as those with $c \geq -0.025$), but is absent for the blue SNe Ia.

As noted at the beginning of this section, we also found a clear trend between the strength of the emission lines and Hubble residuals. When we split the sample according to SN Ia color, we find that red SNe Ia - defined again as those with $c \geq -0.025$ - occur in galaxies with stronger emission lines. These galaxies have higher sSFRs, which have been shown to correlate with dust-to-stellar mass ratios (Orellana et al. 2017; Triani et al. 2021). Similar trends have been found between global/local (U - R) colour and DES5YR Hubble residuals (Kelsey et al. 2022).

Overall, there are hints that dust is playing a role, but the trends are not very significant. Yet, dust is a key part of the BS21 model.

In the BS21 model, the amount of attenuation and the attenuation law, as parameterised by R_V, depends on host galaxy mass. More massive galaxies have shallower attenuation laws but more dust. The model successfully explains the relationships between Hubble scatter and Hubble residuals with SN Ia colour and explains the mass step as a result of the correlation between the galaxy mass and the properties of the dust. The model is consistent with other observations Salim et al. (2018).

The lack of a very significant trend between the amount of reddening inferred from the spectra and Hubble residual is in part due to the limitations of the approach. The reddening inferred from the spectra, which applies to the whole galaxy, may only be weakly correlated to the amount of reddening affecting the supernova.

5.3 Limitations of this analysis and future work

While a number of trends have been shown to exist on stacked spectra, it is unclear how strong they are on individual spectra. This is a limitation of our work. Having higher S/N spectra would allow full spectrum fitting of individual hosts. This is only possible for a small fraction of the host galaxies observed by OzDES and the numbers are too small for clear trends to emerge.

Future surveys, such as TIDES (Swann et al. 2019) on the VISTA telescope at the Paranal Observatory in Chile will obtain spectra of tens of thousands of galaxies that host SNe Ia discovered by the Legacy Survey of Space and Time. This is two orders of magnitude more hosts than analysed here, and the number will be sufficient to see if the trends seen in the stacked spectra are also present when the hosts are analysed individually.

Furthermore, as the seeing is at least a factor of two better than the seeing at Siding Spring, where the AAT is located, and the fibre diamater smaller, the data will probe smaller regions of the host galaxy. For nearby galaxies, it will be possible to measure local properties of the host, as done in Galbany et al. (2018) and Rigault et al. (2020).

Another limitation of our work is the weighting we apply when stacking spectra. More weight is given to brighter objects. We repeated the analysis without weighting and found that the trends remain although with reduced significance.

We also note the insensitivity of the results when α and β are allowed to vary within their uncertainties.

5.4 Impact on Cosmology

5.4.1 The impact on dark energy equation of state

SNe Ia constrain the dark energy equation of state parameter, w, by comparing the luminosity of nearby SNe Ia to distant SNe Ia. In the Pantheon+ SN sample (Brout et al. 2022), distant SNe Ia extend up to $z \sim 2$, which corresponds to a lookback time of ~ 10 Gyr. Over that time, galaxies have evolved significantly. Compared to galaxies today, galaxies 10 Gyr ago were much less massive, less metal rich, bluer, and much more actively forming stars. All of these properties have been shown to correlate with SN Ia Hubble residuals after the standard corrections for light curve width and colour have been applied.

Furthermore, the mean dust attenuation law and the amount of attenuation from dust are also expected to change with increasing look-back time. In high-redshift galaxy analogs (galaxies that sit above the star formation mains sequence), the dust attenuation law is steeper that the law in the Milky Way (Salim et al. 2018). In this paper, we found a marginal trend between Hubble residuals and the Balmer decrement, an indicator of reddening by dust.

While it is not yet clear what drives these trends, left uncorrected, these trends will result in a bias in w. For example, if the age of the progenitor is driving these trends then Childress et al. (2013) find that distant SNe Ia at $z \sim 1$ could be as much as 0.04 mag fainter after light curve and colour correction, corresponding to a change w that is double the current statistical uncertainty in w.

A change in w also results from changes in how the scatter in SNe Ia luminosities after standardisation are modelled. The scatter results in some SNe Ia being preferentially selected over others, which results in a bias that depends, to first order, on redshift. The magnitude of the bias is modelled through detailed simulations (Scolnic & Kessler 2016) and is applied to the distance modulus (see Eq. 2). Over the past decade, the scatter has been modelled phenomenologically with achromatic and chromatic terms contributing to the scatter. The two most common models are the G10 model (Guy et al. 2010), where 80% of the scatter is achromatic and the C11 model (Chotard et al. 2011) where 20% of the scatter is achromatic.

BS21 provide a more physically motivated model for the scatter. The BS21 model allows for an intrinsic relation between SN Ia colour and luminosity and the effects of dust in the host galaxy. In this model, the dust attenuation law, as described by R_V, and the amount of attenuation are allowed to vary and are described by distributions that depend on the properties of the hosts. BS21 find that the mass step is a natural result of the different properties of dust in low and high mass galaxies. BS21 find biases as large as 4% in w between their treatment of the scatter and the treatment of the scatter in the G10 and C11 models. The difference is similar to the statistical uncertainty in w (Brout et al. 2022).

5.4.2 The impact on H_0

For H_0, the absolute brightness of SNe Ia is required. The brightness is calibrated in galaxies that have hosted SNe Ia and are near enough for the distances to be measured independently from the SNe Ia using, for example, Cepheids (Riess et al. 2021), or the tip of the red-giant branch (TRGB)

(Freedman 2021). The SNe Ia that are used to measure the H_0 differ from the ones that are used to calibrate the absolute SN Ia brightness. As the SNe Ia between the two samples differ, so too will the hosts. There is therefore the potential for host-dependent luminosity variations to bias H_0.

Additional H_0 calibrator galaxies will provide improvements in the zero-point calibration of SNe Ia used in determining H_0. However, the number of future candidates will be limited due to the low rate of SN Ia explosions we can detect in nearby galaxies which also contain Cepheids, currently at a rate of ~ 1/year. Recently, an increased sample size of 42 H_0 calibrator galaxies was utilised in the Cepheid approach of calibrating SNe Ia and this reduced each individual error contribution to below 1% (Riess et al. 2021). Cepheids are known to reside in late-type galaxies and this could introduce a bias in the calibration of SNe Ia when comparing to a range of galaxy types at higher redshift which do not contain Cepheids. However, Riess et al. (2016) found that by using a homogeneous sample of late-type galaxies into the Hubble flow, there was no significant change to the uncertainty in measuring H_0. This is due to the much larger Hubble flow sample in comparison to the calibrator galaxies. Recent work on SN Ia sample selection also suggests the benefit of a SNe Ia sample containing bluer SNe Ia as they are less affected by dust and may be more suited for measuring cosmological parameters (Kelsey et al. 2021; González-Gaitán et al. 2021; Meldorf et al. 2022).

As galaxies evolve with redshift, this means the stellar populations of galaxies into the Hubble flow will differ from nearby H_0 calibrator galaxies. As discussed earlier, the sSFR is the most significant Hubble residual step found to date after standard light curve corrections have been applied (Rigault et al. 2020). Recently, Brout et al. (2022) found a sSFR step of 0.031 ± 0.011 in the Pantheon+ SN sample, which then reduced to 0.008 ± 0.011 after applying dust and mass bias corrections (BS21). This suggests that the link between host galaxy mass and dust properties accounts for correlations with host galaxy properties such as the sSFR.

Riess et al. (2021) suggest that while SNe Ia derived distances will be improved by uncovering host galaxy correlations after standardisation of SNe Ia, increasing the size and cross calibrating the calibrator and Hubble flows samples will help mitigate these potential uncertainties in measuring H_0.

5.4.3 Modifying the Tripp equation

Modifying the Tripp equation (Eq. 2) to include the effects of dust explicitly for each SN Ia may be difficult to do in practice with current SN Ia samples. In addition to the determining the SN Ia colour law and the coefficient that relates the strength of correlation between intrinsic colour and luminosity, one needs to determine the dust attenuation law, as parameterised by R_V or some other parameterisation, and the amount of attenuation. Most SNe Ia are observed over a limited wavelength range and in a handful of broadband filters, so it may not be possible to provide meaningful constraints on all the parameters. Most SNe Ia lack observations in the rest frame near-IR, where the impact of dust is smallest and where it is possible, once combined with data in the rest-frame optical, to provide meaningful constraints (Johansson et al. 2021).

A less challenging approach may be to use the host mass

to set R_V and the amount of attenuation to their median values both in the training of the SALT2 light curve model and the fitting of the SN Ia light curves. However, detailed simulations will still be needed to correct for biases in the Hubble diagram.

6 CONCLUSION

Multiple studies have demonstrated that the scatter in the SN Ia Hubble diagram can be reduced by incorporating properties of the host galaxy, such as host galaxy mass, sSFR, and metallicity. Most of these studies have used broad band photometry to infer host properties.

Using a sample 625 SN Ia host galaxies from the DES 5-year photometrically confirmed sample, we search for trends between Hubble residuals and the properties of host galaxies inferred from stacked spectra. We see a clear trend between the strength of the emissions lines (an indicator of the sSFR) and Hubble residual, but find no significant trends between properties inferred from the stellar continuum, such as metallicty, mass-to-light ratio, and age.

We further examine the stacked spectra, searching for a trend between the Balmer decrement (an indicator of reddening by dust) and Hubble residual. We find a marginally significant trend between the $H\gamma/H\beta$ line ratio and Hubble residual. The trend is only present in the redder SNe Ia. This is consistent with the notion that redder SNe Ia are more affected by dust. However, the trends are marginal and a larger sample of SN Ia hosts is required to confirm them.

In the near future, 4MOST will obtain the spectra of tens of thousands of SN Ia host galaxies and will be able to examine the trends detected here with much greater statistical significance.

DATA AVAILABILITY

The DES-SN photometric SN Ia catalogue will be made available as part of the DES5YR SN cosmology analy-

sis at https://des.ncsa.illinois.edu/releases/sn. The OzDES-DR2 spectra utilised in this paper can be publically accessed at: https://docs.datacentral.org.au/ozdes/overview/dr2.

REFERENCES

Betoule M., et al., 2014, A&A, 568, A22
Boone K., et al., 2021, ApJ, 912, 71
Briday M., et al., 2022, A&A, 657, A22
Brout D., Scolnic D., 2021, ApJ, 909, 26
Brout D., et al., 2019a, ApJ, 874, 106
Brout D., et al., 2019b, ApJ, 874, 150
Brout D., et al., 2022, arXiv e-prints, p. arXiv:2202.04077
Campbell H., Fraser M., Gilmore G., 2016, MNRAS, 457, 3470
Cappellari M., 2017, MNRAS, 466, 798
Cappellari M., Emsellem E., 2004, PASP, 116, 138
Childress M., et al., 2013, ApJ, 770, 108
Childress M. J., et al., 2017, MNRAS, 472, 273
Chotard N., et al., 2011, A&A, 529, L4
D'Andrea C. B., et al., 2011, ApJ, 743, 172
DES Collaboration et al., 2016, MNRAS, 460, 1270
Dhawan S., Brout D., Scolnic D., Goobar A., Riess A. G., Miranda V., 2020, ApJ, 894, 54
Domínguez A., et al., 2013, ApJ, 763, 145
Flaugher B., et al., 2015, AJ, 150, 150
Freedman W. L., 2021, ApJ, 919, 16
Galbany L., et al., 2018, ApJ, 855, 107
Galbany L., et al., 2022, A&A, 659, A89
González-Gaitán S., de Jaeger T., Galbany L., Mourão A., Paulino-Afonso A., Filippenko A. V., 2021, MNRAS, 508, 4656
Gupta R. R., et al., 2016, AJ, 152, 154
Guy J., et al., 2010, A&A, 523, A7
Hartley W. G., et al., 2022, MNRAS, 509, 3547
Hoormann J. K., et al., 2019, MNRAS, 487, 3650
Johansson J., et al., 2013, MNRAS, 435, 1680
Johansson J., et al., 2021, ApJ, 923, 237
Johnson B. D., Leja J., Conroy C., Speagle J. S., 2021, ApJS, 254, 22
Kelly P. L., Hicken M., Burke D. L., Mandel K. S., Kirshner R. P., 2010, ApJ, 715, 743
Kelsey L., et al., 2021, MNRAS, 501, 4861
Kelsey L., et al., 2022, Concerning Colour: The Effect of Environment on Type Ia Supernova Colour in the Dark Energy Survey, doi:10.48550/ARXIV.2208.01357, https://arxiv.org/abs/2208.01357
Kessler R., Scolnic D., 2017, ApJ, 836, 56
Khetan N., et al., 2021, A&A, 647, A72
Lampeitl H., et al., 2010, ApJ, 722, 566
Lidman C., et al., 2020, MNRAS, 496, 19
Meldorf C., et al., 2022, The Dark Energy Survey Supernova Program results: Type Ia Supernova brightness correlates with host galaxy dust, doi:10.48550/ARXIV.2206.06928, https://arxiv.org/abs/2206.06928
Möller A., de Boissière T., 2020, MNRAS, 491, 4277
Möller A., et al., 2022, The Dark Energy Survey 5-year photometrically identified Type Ia Supernovae (arXiv:2112.02517)
Morganson E., et al., 2018, PASP, 130, 074501
Orellana G., et al., 2017, A&A, 602, A68
Osterbrock D. E., 1989, Astrophysics of Gaseous Nebulae and Active Galactic Nuclei. University Science Books
Pan Y. C., et al., 2014, MNRAS, 438, 1391
Perlmutter S., et al., 1999, ApJ, 517, 565
Phillips M. M., 1993, ApJ, 413, L105
Pursiainen M., et al., 2020, MNRAS, 494, 5576
Riess A. G., et al., 1998, AJ, 116, 1009
Riess A. G., et al., 2016, ApJ, 826, 56
Riess A. G., et al., 2021, arXiv e-prints, p. arXiv:2112.04510
Rigault M., et al., 2013, A&A, 560, A66
Rigault M., et al., 2020, A&A, 644, A176
Roman M., et al., 2018, A&A, 615, A68
Rose B. M., Garnavich P. M., Berg M. A., 2019, ApJ, 874, 32
Salim S., Boquien M., Lee J. C., 2018, ApJ, 859, 11
Scolnic D., Kessler R., 2016, ApJ, 822, L35
Scolnic D., et al., 2018, ApJ, 859, 101
Smith M., et al., 2020a, AJ, 160, 267
Smith M., et al., 2020b, MNRAS, 494, 4426
Sullivan M., et al., 2010, MNRAS
Swann E., et al., 2019, arXiv: Instrumentation and Methods for Astrophysics
Triani D. P., Sinha M., Croton D. J., Dwek E., Pacifici C., 2021, MNRAS, 503, 1005
Tripp R., 1998, A&A, 331, 815
Uddin S. A., Mould J., Lidman C., Ruhlmann-Kleider V., Hardin D., 2017, Publ. Astron. Soc. Australia, 34, e009
Vazdekis A., Sánchez-Blázquez P., Falcón-Barroso J., Cenarro A. J., Beasley M. A., Cardiel N., Gorgas J., Peletier R. F., 2010, MNRAS, 404, 1639
Wiseman P., et al., 2020a, MNRAS, 495, 4040
Wiseman P., et al., 2020b, MNRAS, 498, 2575
Yuan F., et al., 2015, MNRAS, 452, 3047

APPENDIX A: AUTHOR AFFILIATIONS

[1] Centre for Astrophysics & Supercomputing, Swinburne University of Technology, Victoria 3122, Australia

[2] Centre for Gravitational Astrophysics, College of Science, The Australian National University, ACT 2601, Australia

[3] The Research School of Astronomy and Astrophysics, Australian National University, ACT 2601, Australia

[4] Institute of Cosmology and Gravitation, University of Portsmouth, Portsmouth, PO1 3FX, UK

[5] School of Physics and Astronomy, University of Southampton, Southampton, SO17 1BJ, UK

[6] Center for Astrophysics | Harvard & Smithsonian, 60 Garden Street, Cambridge, MA 02138, USA

[7] Institut d'Estudis Espacials de Catalunya (IEEC), 08034 Barcelona, Spain

[8] Institute of Space Sciences (ICE, CSIC), Campus UAB, Carrer de Can Magrans, s/n, 08193 Barcelona, Spain

[9] School of Mathematics and Physics, University of Queensland, Brisbane, QLD 4072, Australia

[10] Department of Physics, Duke University Durham, NC 27708, USA

[11] Sydney Institute for Astronomy, School of Physics, A28, The University of Sydney, NSW 2006, Australia

[12] Department of Astronomy and Astrophysics, University of Chicago, Chicago, IL 60637, USA

[13] Kavli Institute for Cosmological Physics, University of Chicago, Chicago, IL 60637, USA

[14] Cerro Tololo Inter-American Observatory, NSF's National Optical-Infrared Astronomy Research Laboratory, Casilla 603, La Serena, Chile

[15] Laboratório Interinstitucional de e-Astronomia - LIneA, Rua Gal. José Cristino 77, Rio de Janeiro, RJ - 20921-400, Brazil

[16] Fermi National Accelerator Laboratory, P. O. Box 500, Batavia, IL 60510, USA

[17] Department of Physics, University of Michigan, Ann Arbor, MI 48109, USA

[18] Centro de Investigaciones Energéticas, Medioambientales

y Tecnológicas (CIEMAT), Madrid, Spain

[19] CNRS, UMR 7095, Institut d'Astrophysique de Paris, F-75014, Paris, France

[20] Sorbonne Universités, UPMC Univ Paris 06, UMR 7095, Institut d'Astrophysique de Paris, F-75014, Paris, France

[21] University Observatory, Faculty of Physics, Ludwig-Maximilians-Universität, Scheinerstr. 1, 81679 Munich, Germany

[22] Department of Physics & Astronomy, University College London, Gower Street, London, WC1E 6BT, UK

[23] Kavli Institute for Particle Astrophysics & Cosmology, P. O. Box 2450, Stanford University, Stanford, CA 94305, USA

[24] SLAC National Accelerator Laboratory, Menlo Park, CA 94025, USA

[25] Instituto de Astrofisica de Canarias, E-38205 La Laguna, Tenerife, Spain

[26] Universidad de La Laguna, Dpto. Astrofísica, E-38206 La Laguna, Tenerife, Spain

[27] INAF-Osservatorio Astronomico di Trieste, via G. B. Tiepolo 11, I-34143 Trieste, Italy

[28] Center for Astrophysical Surveys, National Center for Supercomputing Applications, 1205 West Clark St., Urbana, IL 61801, USA

[29] Department of Astronomy, University of Illinois at Urbana-Champaign, 1002 W. Green Street, Urbana, IL 61801, USA

[30] Institut de Física d'Altes Energies (IFAE), The Barcelona Institute of Science and Technology, Campus UAB, 08193 Bellaterra (Barcelona) Spain

[31] Astronomy Unit, Department of Physics, University of Trieste, via Tiepolo 11, I-34131 Trieste, Italy

[32] Institute for Fundamental Physics of the Universe, Via Beirut 2, 34014 Trieste, Italy

[33] Hamburger Sternwarte, Universität Hamburg, Gojenbergsweg 112, 21029 Hamburg, Germany

[34] Jet Propulsion Laboratory, California Institute of Technology, 4800 Oak Grove Dr., Pasadena, CA 91109, USA

[35] Institute of Theoretical Astrophysics, University of Oslo. P.O. Box 1029 Blindern, NO-0315 Oslo, Norway

[36] Instituto de Fisica Teorica UAM/CSIC, Universidad Autonoma de Madrid, 28049 Madrid, Spain

[37] Department of Physics and Astronomy, University of Pennsylvania, Philadelphia, PA 19104, USA

[38] Department of Astronomy, University of Michigan, Ann Arbor, MI 48109, USA

[39] Observatório Nacional, Rua Gal. José Cristino 77, Rio de Janeiro, RJ - 20921-400, Brazil

[40] Santa Cruz Institute for Particle Physics, Santa Cruz, CA 95064, USA

[41] Center for Cosmology and Astro-Particle Physics, The Ohio State University, Columbus, OH 43210, USA

[42] Department of Physics, The Ohio State University, Columbus, OH 43210, USA

[43] Australian Astronomical Optics, Macquarie University, North Ryde, NSW 2113, Australia

[44] Lowell Observatory, 1400 Mars Hill Rd, Flagstaff, AZ 86001, USA

[45] Institució Catalana de Recerca i Estudis Avançats, E-08010 Barcelona, Spain

[46] Physics Department, 2320 Chamberlin Hall, University of Wisconsin-Madison, 1150 University Avenue Madison, WI 53706-1390

[47] Department of Physics, University of Surrey, Guilford, Surrey, UK

[48] Department of Astronomy, University of California, Berkeley, 501 Campbell Hall, Berkeley, CA 94720, USA

[49] Institute of Astronomy, University of Cambridge, Madingley Road, Cambridge CB3 0HA, UK

[50] Department of Astrophysical Sciences, Princeton University, Peyton Hall, Princeton, NJ 08544, USA

[51] Department of Physics and Astronomy, Pevensey Building, University of Sussex, Brighton, BN1 9QH, UK

[52] Computer Science and Mathematics Division, Oak Ridge National Laboratory, Oak Ridge, TN 37831

[53] Excellence Cluster Origins, Boltzmannstr. 2, 85748 Garching, Germany

[54] Max Planck Institute for Extraterrestrial Physics, Giessenbachstrasse, 85748 Garching, Germany

[55] Universitäts-Sternwarte, Fakultät für Physik, Ludwig-Maximilians Universität München, Scheinerstr. 1, 81679 München, Germany

This paper has been typeset from a TeX/LaTeX file prepared by the author.